THE JOURNAL OF PHYSICAL CHEMISTRY C
A JOURNAL OF THE AMERICAN CHEMICAL SOCIETY

pubs.acs.org/JPCC
Article

Reproduction of Chiral Anisotropy in Surface-Enhanced Raman Scattering on Gold Nanowires by Computational Modeling

Ondřej Škrna, Jiří Kessler, Zexi Liu, Shunai Che, and Petr Bouř*

Cite This: J. Phys. Chem. C 2024, 128, 12649−12656
Read Online

ACCESS | Metrics & More | Article Recommendations | Supporting Information

ABSTRACT: Chiral gold nanostructured films were found to exhibit extremely strong surface-enhanced Raman scattering chiral anisotropy, but the physical origin of this phenomenon remained a mystery. In the present study, a robust model is presented, revealing properties of the gold wires important for the interaction with the analytes and discrimination of molecular enantiomers. Molecular dynamics and quantum chemical computations are utilized; the enhanced electromagnetic field of gold clusters is treated without a multipole approximation. The simulations show that the gold self-polarization produces a static electric field reflecting the chiral symmetry of the nanowires; it significantly enhances the geometrical preference for the enantiomers and affects how the analyte is distributed along the nanostructure surface. The electro-mechanical sensitivity is further amplified by the strongly nonlinear Raman response to the laser excitation in resonance. The current computational approach is limited by the size of the system, but it is amendable to improvement and the rationalization increases the potential of SERS-ChA as a powerful analytical method for chirality detection in chemistry, biology, and the environment.

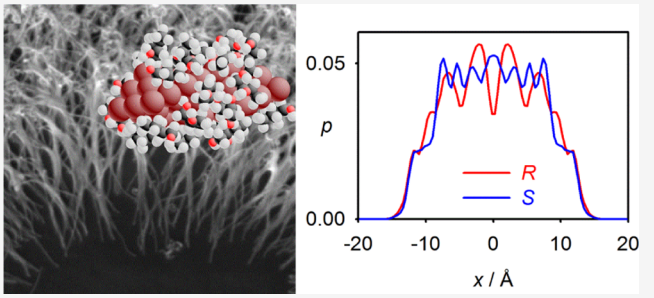

INTRODUCTION

Determination of the absolute configuration, enantiomeric excess, and other aspects of molecular chirality is essential to many fields including asymmetric chemical synthesis, medicine, biochemistry, and material science. Many methods exploring linearly or circularly polarized light have been developed for this purpose, starting with L. Pasteur's optical rotation (OR).[1] However, the chiral interaction of the light with molecules is rather weak, essentially reflecting the small ratio of molecular size and the light wavelength. The weakness significantly complicates the chirality detection.[2]

Therefore, the observation that "simple" surface-enhanced Raman scattering (SERS) on chiral nanostructured Au films (CNAFs) is sensitive to chirality attracted much attention.[3,4] For this SERS chiral anisotropy (SERS-ChA), the polarization of the light was not needed, and still, the *g*-factors were often close to the maximal value of two. They are defined as $g = 2|I_S - I_R|/(I_S + I_R)$, where $I_{S/R}$ is the SERS intensities for opposite enantiomers. Note that analogous measures in most methods exploring differential interaction of molecules with circularly polarized light are much smaller. For instance, typical *g*-values of electronic circular dichroism (ECD) or vibrational optical activity (VOA) are about 10^{-3} and 10^{-4}.[5] In the present study, we focus on the physical substance and possibility to model the SERS-ChA effect necessary for its wider applications. Except for very special cases, we did not reproduce the almost ideal chiral discrimination ($g \sim 2$) seen experimentally, but the predicted *g*-factors approach this value, i.e., being by a few orders larger than for usual chiroptical spectroscopies.

The SERS-ChA methodology thus has a chance to complement other techniques exploiting or detecting molecular chirality.[2,6−8] Its advantages would also include relative independence of detailed chemical composition, while, for example, spectroscopies utilizing electronic transitions [OR, optical rotatory dispersion (ORD), ECD, circularly polarized luminescence (CPL)] require suitable chromophores.[9] These chiroptical signals are also quite dependent on the concentration, solvent, and other experimental parameters, which are all difficult to simulate. The simulations are easier for VOA including vibrational circular dichroism (VCD) and Raman optical activity (ROA), where only the electronic ground states are normally needed.[5] However, vibrational transitions provide a much weaker response to circularly polarized light than electronic ones; the experiments are lengthier and require expensive instrumentation.[10] A more sensitive surface-enhanced ROA spectroscopy has also been proposed, but currently, it has limited applicability and reliability.[11,12]

Received: April 25, 2024
Revised: July 3, 2024
Accepted: July 5, 2024
Published: July 18, 2024

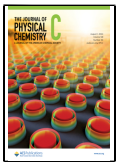

https://doi.org/10.1021/acs.jpcc.4c02703
J. Phys. Chem. C 2024, 128, 12649−12656

The preparation of CNAFs is relatively straightforward; they were grown on silicon-containing wafers from Au^{3+} solutions in the presence of N-acetylcysteine as a symmetry-breaking agent. At the final stage, long gold wires were formed, about 4 nm in diameter, and the atoms formed the Boerdijk−Coxeter−Bernal (BCB) helix. This structure can also be imagined as a chain of gold tetrahedrons.[13]

The chiral SERS effect, however, is rather complex. The chiral discrimination was vaguely related to the electromagnetic properties of CNAFs without further elaboration.[3] Here, we suggest a more explicit model explaining many of the observed trends. Dynamic CNAFs' electric field is computed ab initio without any multipole approximation. The interactions between model chiral molecules and gold wires are explored by means of molecular dynamics. The results indicate the importance of the geometry factors, and further differences in SERS intensities caused by two enantiomers absorbed on the wire surface are ascribed to different perturbations of the gold electronic levels. The electronic structure affects the polarizabilities of the nanowires and consequently the dynamic electromagnetic field responsible for the enhancement of the Raman signal. Although the size of the model systems (already significantly reduced compared to that of the experiment) does not allow for very accurate quantum chemical level calculations, the modeling already provides significant anisotropy ratios close to those observed in the experiment and deep insight into the physical basis of SERS-ChA.

THEORY

We are interested in the enhancement η of the detected Raman intensity of an analyte in the presence of the wire compared to the case of the isolated molecule. We adopt the generally accepted simplification that η is proportional to the fourth power of the intensity of the electromagnetic field,

$$\eta = (E/E_i)^4 \tag{1}$$

where E and E_i are the electric field intensities at the molecule with and without the wire, respectively. This dependence comes from the polarization of the molecule by the excitation light interacting with the wire as well as from an analogous interaction of the outgoing radiation.[14]

The system "wire + close molecules" is polarized due to the dynamic, time-dependent electromagnetic field of the excitation light. From the Maxwell equations, we obtain the electric field at position $\boldsymbol{R}$ as[2]

$$\boldsymbol{E}(\boldsymbol{R}, t)\frac{1}{4\pi\varepsilon_0}\int\frac{(\boldsymbol{R}-\boldsymbol{r})\rho(\boldsymbol{r}, t)}{|\boldsymbol{R}-\boldsymbol{r}|^3}\mathrm{d}\boldsymbol{r} \tag{2}$$

where ε_0 is the vacuum permittivity, $\rho(\boldsymbol{r}, t)$ is the dynamic electron density of the wire, and t is the time. The density can be obtained from the electronic wave function ψ as

$$\rho(\boldsymbol{r}, t) = -eN\int\psi^*\psi\,\mathrm{d}r_2 \ldots \mathrm{d}r_N\mathrm{d}\boldsymbol{s} \tag{3}$$

where e is the electronic charge (taking $e > 0$), N is the number of electrons, and we integrate over all spins ($\mathrm{d}\boldsymbol{s}$) and all spatial coordinates of all electrons except one.

The interaction between the electrons and the excitation light is described by the potential[2]

$$V(t) = \frac{e}{m}\sum_{i=1}^{N}\boldsymbol{p}_i\cdot\boldsymbol{A}(\boldsymbol{r}_i, t) \tag{4}$$

where $\boldsymbol{p}_i$, $\boldsymbol{r}_i$, and m are the electronic momenta, positions, and mass, respectively, and $\boldsymbol{A}$ is the vector potential. Since the dimension of our system is still smaller than the wavelength of the laser light (typically 532 nm),[3] we consider $\boldsymbol{A}$ to be constant in space, $\boldsymbol{A}(\boldsymbol{r}_i,t) \cong \boldsymbol{A}(\boldsymbol{0},t)$, where $\boldsymbol{0}$ is the position of the mass center. From the Maxwell equations, assuming plane waves, we get $\boldsymbol{E} = -\dot{\boldsymbol{A}}$ and $\boldsymbol{A}(\boldsymbol{0},t) = \omega^{-1}\boldsymbol{E}_0\cos(\omega t)$ so that

$$V(t) = v e^{i\omega t} + v^* e^{-i\omega t} \tag{5}$$

where $v = \frac{e}{2m\omega}\sum_{i=1}^{N}\boldsymbol{p}_i\cdot\boldsymbol{E}_0$, $\boldsymbol{E}_0$ is the electric field of the excitation radiation at $t = 0$, and ω is the angular frequency of the light. Knowing unperturbed ground φ_0 and excited φ_n wave functions, the perturbed ground state can be approximated by[15]

$$\psi = \varphi_0(t) + \sum_n c_n(t)\varphi_n(t) \tag{6}$$

where coefficients $c_n = \frac{v_{n0}}{\hbar}\frac{e^{i(\omega_{n0}-\omega)t}}{\omega-\omega_{n0}}$, $\hbar$ is the reduced Planck constant, $\omega_{n0} = \omega_n - \omega_0$ is the difference between excited and ground-state frequencies, and $v_{n0} = \langle\varphi_n(0)|v|\varphi_0(0)\rangle$. From (3) and (6) for real wave functions, we get

$$\rho(\boldsymbol{r}, t) = \rho_0 - \frac{eN}{\hbar}\sum_n\frac{1}{\omega-\omega_{k0}}(v_{n0}e^{-i\omega t} + v_{n0}^* e^{i\omega t})\int\varphi_n(0)\varphi_0(0)\mathrm{d}r_2 \ldots \mathrm{d}r_N \tag{7}$$

where $\rho_0 = -eN\int\varphi_0^*\varphi_0\mathrm{d}r_2\cdots\mathrm{d}r_N$ is the static charge density.

Next, we use the dipole-velocity transformation, $\left\langle\varphi_n(0)\middle|\sum_{i=1}^{N}p_{i\beta}\middle|\varphi_0(0)\right\rangle = \frac{im\varepsilon_{n0}\mu_{\beta n0}}{\hbar e}$, where $\mu_\beta = \sum_{i=1}^{N}er_{i\beta}$ is the dipole moment operator and $\mu_{\beta n0} = \langle\varphi_n(0)|\mu_\beta|\varphi_0(0)\rangle$. For the excitation radiation polarized along the β-axis ($\boldsymbol{E}_{0,\beta} = E_0$), we get $v_{n0} = \frac{i}{2}\mu_{\beta n0}E_0$, and

$$\rho(\boldsymbol{r}, t) = \rho_0 - \frac{eN}{\hbar}\sum_n\frac{\mu_{\beta n0}}{\omega-\omega_{k0}}\sin(\omega t)E_0\int\varphi_n(0)\varphi_0(0)\mathrm{d}r_2 \ldots \mathrm{d}r_N \tag{8}$$

For actual quantum chemical computations, we suppose a closed shell, the ground state is described by the Slater determinant $\varphi_0 = \Delta_0$, and the excited states are $\varphi_n = \sum_{a,\mathrm{occ.}}\sum_{b,\mathrm{virt.}}c_{ab}^n\tilde{\Delta}_{ab}$, where c_{ab} are the configuration interaction (CI) coefficients and $\tilde{\Delta}_{ab} = (\Delta_{ab}^{\alpha} - \Delta_{ab}^{\beta})/\sqrt{2}$ is the singlet spin-adapted combination of the Slater determinants; $\Delta_{ab}^{\alpha/\beta}$ is made from Δ_0, where the electron with spin α/β is moved from an occupied orbital a to a virtual one b. Then, the integral in (8) becomes

$$\int\varphi_0(0)\varphi_n(0)\mathrm{d}r_2 \ldots \mathrm{d}r_N = \frac{1}{\sqrt{2}N}\sum_{a,\mathrm{occ.}}\sum_{b,\mathrm{virt.}}c_{ab}^n a(\boldsymbol{r})b(\boldsymbol{r}) \tag{9}$$

Putting (2) and (8) together, the time-dependent part of the electric field is

https://doi.org/10.1021/acs.jpcc.4c02703
J. Phys. Chem. C 2024, 128, 12649−12656

$$\boldsymbol{E}(\boldsymbol{R}, t) = \frac{-eE_0}{4\sqrt{2}\hbar\pi\varepsilon_0}\sin(\omega t)\sum_n \frac{\mu_{\beta n0}}{\omega - \omega_{k0} + i\Gamma} \sum_{a,\mathrm{occ.}}\sum_{b,\mathrm{virt.}} c_{ab}^n \mathbf{I}_{ab} \tag{10}$$

where $\boldsymbol{I}_{ab} = \int \frac{(\boldsymbol{R}-\boldsymbol{r})a(\boldsymbol{r})b(\boldsymbol{r})}{|\boldsymbol{R}-\boldsymbol{r}|^3}\mathrm{d}\boldsymbol{r}$. As usual, to avoid divergence of the intensity,[16,17] we introduced a complex frequency uncertainty $i\Gamma$, with $i = \sqrt{-1}$. Dividing (10) by the initial field $E_0 \sin(\omega t)$, we get the enhancement for a β-polarization as

$$\eta_\beta = \left| \frac{e}{4\sqrt{2}\hbar\pi\varepsilon_0} \sum_n \frac{\mu_{\beta n0}}{\omega - \omega_{k0} + i\Gamma} \sum_{a,\mathrm{occ.}}\sum_{b,\mathrm{virt.}} c_{ab}^n \boldsymbol{I}_{ab} \right|^4 \tag{11}$$

For simplicity, we report the average, $\eta = (\eta_x + \eta_y + \eta_z)/3$ since it is difficult to maintain a fixed orientation in the experiment. Note that for the electric field in (10), a multipole expansion is not applicable since the dimensions of the wire and the system $(\boldsymbol{R}, \boldsymbol{r})$ are comparable. The two-electron integrals can be calculated in a standard way,

$$\boldsymbol{I}_{ab} = -\left(\frac{\delta}{\pi}\right)^{3/2} \frac{\partial(ab/cd)}{\partial \boldsymbol{R}} \tag{12}$$

for $\gamma \to 0$, $\delta \to \infty$, where $(ab|cd)$ is the usual two-electron repulsion integral.[18] From the enhancements for R and S enantiomers (η_R, η_S), we obtain the g-factors,[3]

$$g = 2(\eta_\mathrm{R} - \eta_\mathrm{L})/(\eta_\mathrm{R} + \eta_\mathrm{L}) \tag{13}$$

varying from 0 (no chiral discrimination) to the maximum of 2.

QUANTUM CHEMICAL CALCULATIONS

The enhancements were calculated for various gold clusters—"wires"—and their complexes with chiral analytes. Geometries of the wires in the form of BCB helices were created by our own software, differing in sides (number of atoms along, l, determining also the overall twist) of the basic equilateral triangle and the total number of atoms: Au_{46} (with $l = 3$), Au_{120} ($l = 4$), Au_{314} ($l = 5$), and Au_{420} ($l = 7$).

The electric field was calculated at the distance of 4 Å from the gold surface on an ensemble of Lebedev–Laikov points[19] and averaged. The points were placed on spheres originating at surface gold atoms. An averaging over the mass centers of the studied molecules provided similar results. The Gaussian software[20] was used for quantum chemical computations. The excited states were constructed in several ways. As the most advanced model, time-dependent density functional theory (TDDFT) was used with the B3LYP[21] functional and 6-31G** basis set for the absorbed molecules. For gold, the LANL2DZ[22] effective core potential and basis set were applied. The MWB60[23] potential was also tried, giving almost the same results in a longer computational time. As simplified models, TDDFT and CIS[24] approaches were used with the PM7[25] semiempirical Hamiltonian.

The simplest models of the electron excited states were based on rigid orbitals and B3LYP, PM7, or Hückel[26] ground-state Slater determinants. Then, transition energies were obtained as differences between virtual and occupied orbital energies, and the transition dipole moments $(\mu_{\beta \mathrm{on}})$ were obtained as transition integrals between molecular orbitals. To make the transition wavelengths λ more realistic, a scaling in the form of $\lambda' = \lambda_{\max}\sqrt{\lambda/\lambda_{\max}}$ was applied, where $\lambda_{\max}$ is the position of the absorption maximum. Similarly, the transition dipole moments d, calculated too large for long wavelengths at this level, were transformed as $d' = d \times \exp[-(\lambda - \lambda_{\max})^2/\Delta^2]$, where Δ = 400 nm. These scalings had minor effects on the results, as the excitation frequencies were always set close to the absorption maxima. Examples of absorption spectra for different approximations are given in Figure S3. Using these models, the enhancement factors were calculated as detailed above.

Molecular dynamics (MD) was run within the Tinker[27] or Amber[28] software, giving similar results. To investigate the interaction of the analytes with the gold surface, a gold cluster in the form of the BCB helix has been submerged into a box filled with the solvent (2-butanediol, phenylglycine, glyceraldehyde, or 1,2-epoxybutane),and after an equilibration stage, geometry snapshots were created each 1 ps. The gold atoms were represented by the Lennard–Jones potentials, partial atomic charges were calculated according to the Merz–Singh–Kollman scheme[29] at the B3LYP/LANL2DZ level, and atomic positions were kept fixed. In the snapshots, only solvent molecules closer than 3.6 Å were left, the geometry was optimized using the same force field as for the dynamics, and the average enhancement factors were calculated as detailed above. For larger gold clusters (Au_{120}, Au_{314}, Au_{420}), the charges used in MD were obtained at lower approximation levels (HF, PM7).

To describe the chirality stemming from the molecular orientation with respect to the gold surface, we introduce a plane chirality index. For a solvent molecule of mass center $\boldsymbol{r}_m$, we define the closest gold atom of position $\boldsymbol{r}_a$ and the distance vector $\boldsymbol{z}_m = \boldsymbol{r}_m - \boldsymbol{r}_a$. Within the plane perpendicular to $\boldsymbol{z}_m$, we define $\boldsymbol{x}$ and $\boldsymbol{y}$ coordinate axes and calculate projections of coordinates of atoms i belonging to this molecule to the plane (x_i, y_i), with the coordinate origin at $\boldsymbol{r}_m$. Then, the index is

$$\chi_m = \left(\sum_{i\in m} Z_i^2\right)^{-1} \sum_{i\in m}\sum_{j\in m, r_j > r_i} Z_i Z_j \frac{x_i y_j - y_i x_j}{r_{ij}^2} \tag{14}$$

and its radial dependence $\chi(r) = \frac{V}{4\pi d N}\sum \frac{\chi_m}{z_m^2}$, where Z_i are the atomic numbers, V is the volume of the simulation box, N is the number of molecules, and we sum over molecules m with distances within $(r, r + d)$.

RESULTS AND DISCUSSION

According to the results, self-polarization of the nanowires is essential for SERS-ChA. This is consistent with previous works, e.g., indicating an important role of the spontaneous polarization for gold colloid aggregation.[30−32] The gold arranged in the BCB helix polarizes itself and gives rise to a significant electrostatic field close to the surface. This was relatively difficult to predict for larger systems because the computational time steeply increases with the size. In particular, the self-consistency in the Hartree–Fock or Kohn–Sham computations of the energies was quite difficult to achieve. However, for limited models, the polarization patterns could be obtained, and some examples are given in Figure 1.

In the figure, we compare the surface electrostatic potentials of three model helices; three quantum chemical models are used. It is important to realize that the triangles on the surface

https://doi.org/10.1021/acs.jpcc.4c02703
J. Phys. Chem. C 2024, 128, 12649−12656

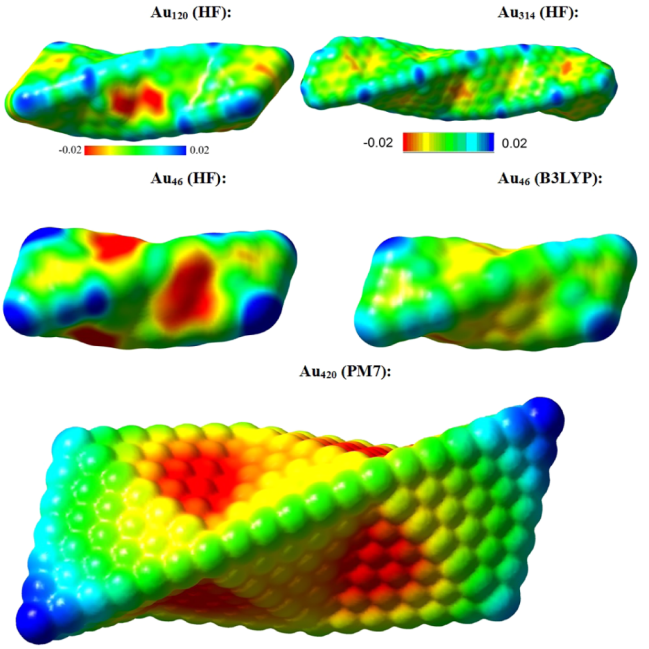

Figure 1. Examples of the self-polarization of the gold clusters. The electrostatic potentials (a.u.) on the isodensity surfaces (ρ = 0.0004 au) of model BCB helices (Au_{46}, Au_{120}, Au_{314}, and Au_{420} clusters) were calculated by the methods indicated. The HF and B3LYP results are for the LANL2DZ basis set and the pseudopotential. Blue/red regions indicate positive/negative potentials; for PM7, the calculated potential was multiplied by 0.2 to plot it at the same scale.

of a long helix are all the same; shorter models obviously introduce some terminal perturbations. However, each side of the triangle is different, which is the necessary condition for surface chirality.[33] At the concave boundary of neighboring triangles, we see a pocket of negative charge (red); the outer edge boundary is positive (blue), while the inner edges are neutral/slightly positive (green). Thus, the geometrical chirality is imprinted into a more local electrostatic pattern. The corresponding electrostatic field-fitted partial atomic charges[29] vary approximately within −0.2···0.2. The potential predicted for the Au_{46} cluster by the B3LYP functional is more uniform than that from the HF method, but the principal pattern is conserved. For Au_{420}, the PM7 method predicts a much stronger electrostatic potential than for the smaller clusters.

During SERS, exciting laser light strongly polarizes the nanostructures. Another key element in the simulation is thus the reproduction of the time-dependent (dynamic) electric field intensities. For the Au_{46} and Au_{420} models, the calculated fields are plotted in Figure 2. For Au_{46}, TDDFT and Hückel calculations are compared. With TDDFT, larger intensity is obtained on average, indicating that the Hückel approximation underestimates the dynamic polarizability. This is unfortunate since TDDFT computational demands are prohibitive for the treatment of larger systems. Still, we found this and other simpler methods usable to at least qualitatively predict the behavior of the wires in the laser field. They are immensely fast. For example, while the B3LYP/LANL2DZ computation of 700 electronic excited states of Au_{46} takes 65 days (one Intel Xeon CPU E5-2630 @ 2.40 GHz), analogous Hückel orbital—based computation takes several minutes only. As may be expected, for the bigger Au_{420} cluster, the dynamic field is stronger and extends farther from the gold surface than for Au_{46}. The field enhancements predicted with the PM7-reduced (rigid orbital) and Hückel models are similar, although the detailed patterns differ. For example, PM7 gives a stronger field on the edges of Au_{420}. Since the Hückel method is much faster than PM7, we use it as a default.

Rather surprising was a relatively strong "mechanical" chiral discrimination, i.e., some parts of the wires preferentially attracted one enantiomer. This can be demonstrated for a gold wire of 46 atoms submerged in *R* and *S* butanediols. Using MD, we calculated the average relative solvent density (g_A) as being dependent on the distance from the gold surface. This function is roughly analogous to the radial distribution function. As another measure, we explore the chirality index

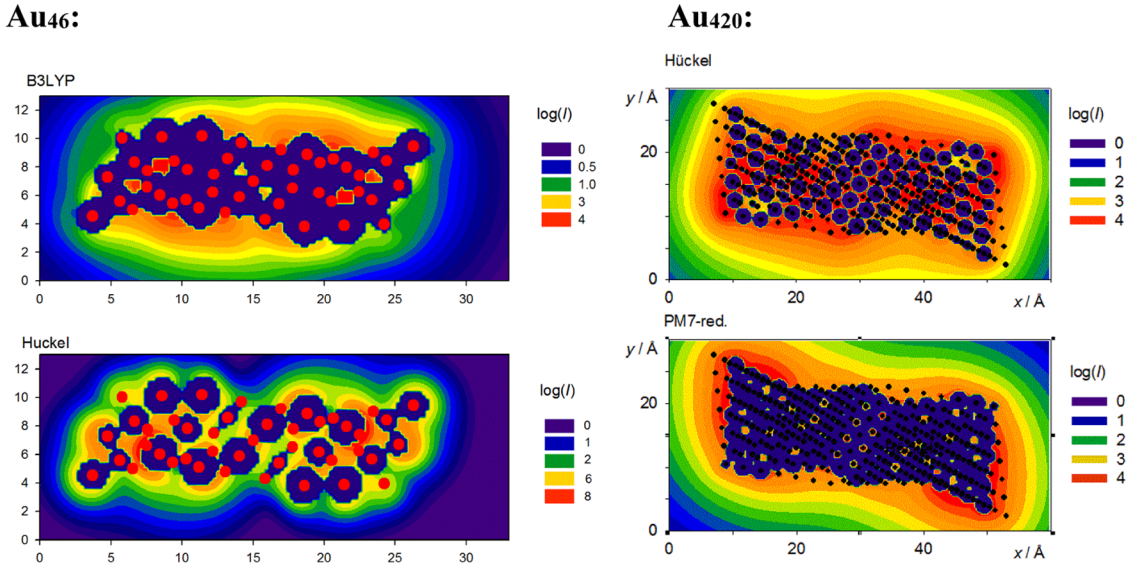

Figure 2. Dynamic electric field under laser excitation. Electric field intensities in cross sections of the Au_{46} (left) and Au_{420} (right) clusters, calculated with the excitation wavelength close to the plasmon absorption maxima, for excitation polarization along the *x* horizontal axis, TDDFT and Hückel (Au_{46}), and Hückel and PM7 (Au_{420}) computations.

https://doi.org/10.1021/acs.jpcc.4c02703
J. Phys. Chem. C 2024, 128, 12649−12656

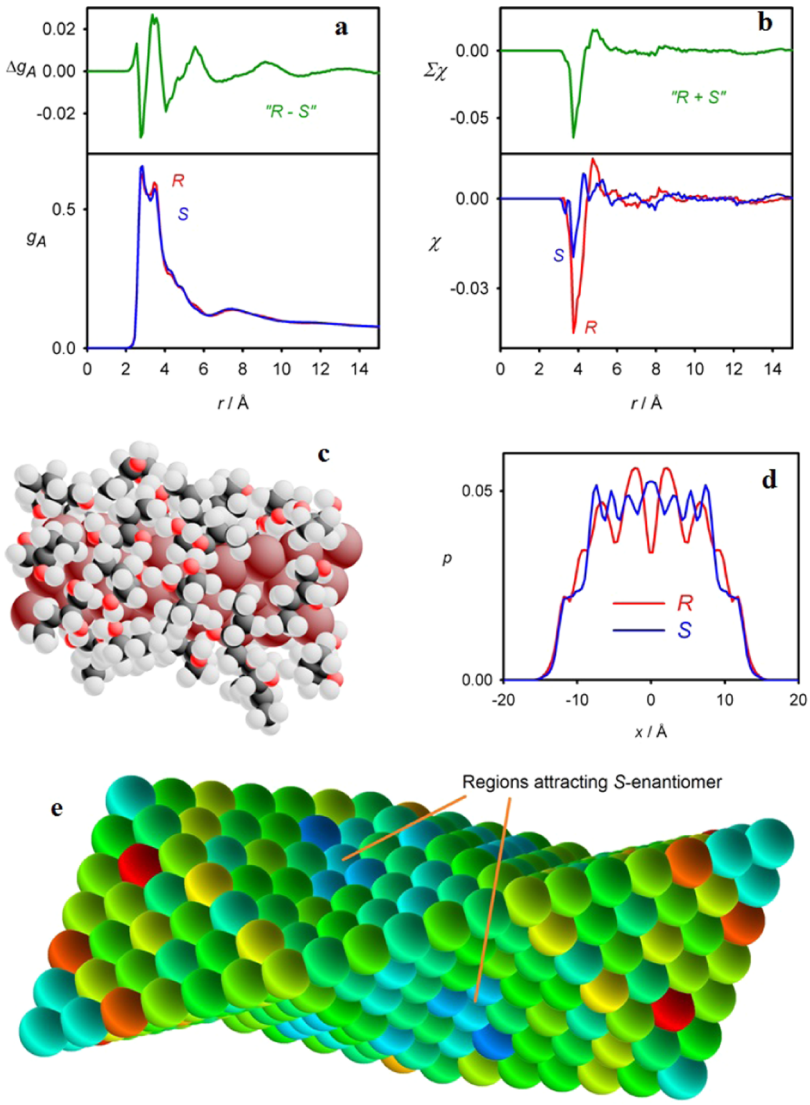

Figure 3. Mechanical preference for enantiomers of *R* and *S* butanediols. (a) Solvent distribution functions and (b) chirality indices dependent on the distance from the gold surface, (c) example of the first solvation sphere, (d) average probability distribution of the analyte along the wire axis, and (e) relative density difference in the vicinity of Au atoms; *R*/*S* attracting regions are in red/blue. 100 000 (e), 10 000 (a, b), and 1000 (d) snapshot averages are displayed, a–d for Au_{46}, e for Au_{420}.

sensitive not only to density but also to molecular chirality. As can be seen in Figure 3a,b, the densities of the butanediol enantiomers differ only in a minor way in the vicinity of the gold surface. The chirality indices (cf. eq 14) differ more for the *R* and *S* forms, which suggests that interaction with the gold strongly affects molecular orientation and local surface chirality.

To better mimic the actual Raman experiment where the analyte remains on the surface while a solvent (usually chloroform) is evaporated,[3] we adopted a simple model leaving only the first hydration sphere. In it, butanediol molecules far from the gold surface were deleted from many MD snapshots, as in the example in Figure 3c. After averaging such geometries, the resultant solvent distribution probability along the wire axis (x) also indicates significant differences between the *R* and *S* butanediols (Figure 3d). Various parts of the gold wires have clearly different affinities for the *S* and *R* enantiomers. In the displayed example, the center of the gold "wire" is preferentially occupied by the *S*-form. In both cases, the largest differences in the *S*/*R* distributions are predicted close to the center of the gold, which can be related to the helical chirality, while the ends interact with the solvent in a rather nonchiral way. Analogous results were obtained for a larger 120-atom gold cluster (Figure S1 in the Supporting Information) with different force fields and analyte molecules.

Another indicator of the mechanical chiral sensitivity may be the local solvent density. For the MD trajectories, we noticed small but detectable differences in average densities of the *R* and *S* enantiomers in the vicinity of particular gold atoms. An example of the Au_{420} cluster submerged in the butanediols is plotted in Figure 3e. For this figure, an average number of solvent atoms around each atom of gold (closer than 8 Å) was counted as obtained in 100 ns MD runs from 100 000 snapshots equally separated in time. The numbers for the *S* and *R* solvents were subtracted and assigned a false color scale. Although the differences are tiny, we can see that the gold atoms close to the concave inner edges "attract" the *S*-form more than the *R*-one.

The dynamic electric field of the gold is quite sensitive to interaction with molecules on the surface. The detected

https://doi.org/10.1021/acs.jpcc.4c02703
J. Phys. Chem. C 2024, 128, 12649−12656

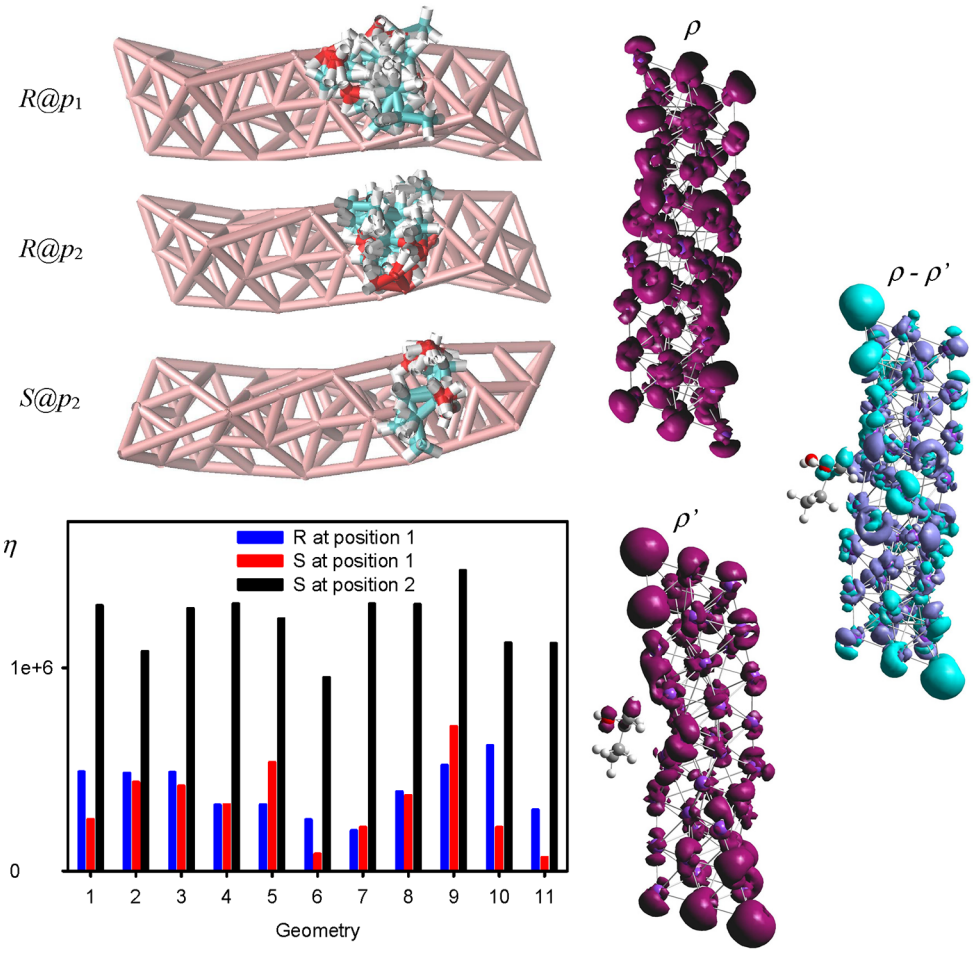

Figure 4. Sensitivity of Raman scattering on the position (p_1 and p_2, closer and farther from the cluster center) of the analyte. (Left) Ten MD snapshots of one *R*/*S* butanediol placed in two positions of Au_{46} cluster, calculated SERS enhancement factors η, (right) dynamic density calculated without and with a *S* butanediol molecule (ρ and ρ', respectively) and the difference. TDDFT B3LYP/6-31G**/LANL2DZ calculation.

molecules produce or lay in different dynamic electric fields, and this difference is further magnified by the steep dependence of the enhancement factors (η) on the electric intensity (eq 1).[14] In Figure 4, the factors calculated at molecular mass centers are compared for various geometries of *R* and *S* butanediols placed ad hoc at the surface. A short 100 ps dynamics was run to obtain a distribution of butanediol geometries. During this time, the molecule did not leave the original pocket of the gold wire. The enhancements in position 2 are clearly about 2−3 times bigger than for position 1. For position 1, however, the enhancements for the *R* and *S* enantiomers are about the same, within the statistical error. A relatively long computational time (∼36 days at one processor for one geometry, 220 excited states involved) does not allow us to compute too many geometries. Nevertheless, the results show the importance of the geometry factor in chiral SERS discrimination. Computations with larger basis sets give larger enhancement and the chiral discrimination (*g*) factors (Table S1). For the aug-cc-pVTZ basis set, the calculated enhancement (∼10^7) and *g*-factor (∼2) perfectly correspond to values observed in SERS experiments.[3] Unfortunately, this level does not allow for the treatment of larger systems and for obtaining proper statistics on a large ensemble of the snapshots.

In Figure 4, we can also see that the analyte molecule causes a perturbation of the dynamic density extended over the whole gold cluster. Large density variations not only appear in the vicinity of butanediol but also rather far from it at the wire's tips. We compare this effect to a "stinging wasp", affecting the whole body. Here, the local interaction translates into changes in the dynamic electric field along the entire wire (cf., Figure S2 for alternate representation). The surface interaction propagates through the gold cluster and affects its properties far from the interaction site.

Putting the findings discussed above together, we proposed the computational scheme overviewed in Figure 5, allowing us to understand how the geometric and resonance-SERS effects can lead to a macroscopically observable chiral anisotropy, that is, significant SERS intensity variations for different enantiomers. The generation of MD snapshots and the first solvation sphere mimics the injection of the analyte onto the gold nanostructures, while the dynamic electromagnetic field is calculated directly using the quantum mechanical models. Indeed, for a range of molecules and gold clusters, the resultant *g*-factors clearly indicate a measurable effect. Examples of calculated enhancements and *g*-factors are listed in Table 1, and more systems are included in Table S2. The factors are lower than experimental ones, the latter often close to the maximum value of two,[3] nevertheless convincingly demonstrating the viability of the adopted model to capture the chiral discrimination.

It should be noted that the formal errors of the averages in Table 1 are somewhat dependent on the computational details,

https://doi.org/10.1021/acs.jpcc.4c02703
J. Phys. Chem. C 2024, 128, 12649−12656

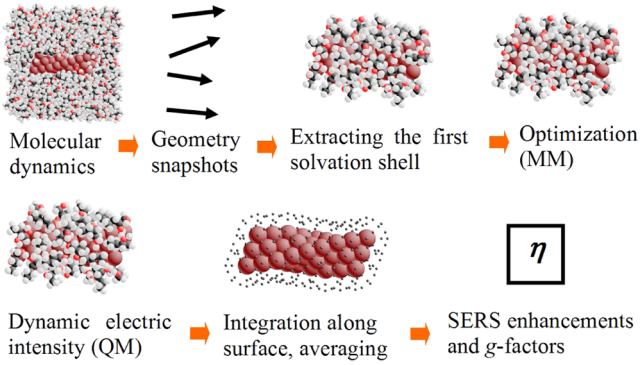

Figure 5. Computational flow to model the SERS-ChA effect. Molecular dynamics runs produce snapshot geometries; in each, the first hydration shell was considered and optimized at the molecular mechanics level. For this system, the dynamic electric intensity was calculated at a quantum mechanical level at a Lebedev−Laikov grid 4 Å above the surface, averaged over the grid points, spatial orientations (x, y, z polarizations), and snapshots.

such as the number of snapshots or points averaged. Nevertheless, the results convincingly show that the computational protocol from Figure 5 reproduces chiral discrimination. In addition, it allows us to demonstrate the effect of the gold autopolarization: as can be seen in Figure 6, the effective partial atomic charges are quite essential for the SERS-ChA effect.

CONCLUSIONS

We see the three most interesting aspects of the results coming from the molecular dynamics and quantum chemical modeling: (1) We could reproduce the SERS-ChA experiment and relate it to the chirality-recognition and resonance Raman phenomena. (2) We implemented and tested the DFT-based methodology producing the dynamic electromagnetic field of molecules without a multipole approximation, which can be generally used for similar SERS nanostructured substrates. (3) Finally, the modeling reveals some specific properties of the BCB gold helix, such as the self-polarization and electromechanical chiral discrimination when interacting with chiral analytes.

At the same time, significant challenges appear for the future, such as the need for a more accurate treatment of the electronic wave function. In the present study, serious simplifications of the quantum chemical models were necessary, given by the availability of computational resources. Adopting more accurate approaches, such as TDDFT instead of the rigid orbital Hückel model or using a larger basis set, can lead to a dramatic increase of the enhancement and g-factors. In addition, we are aware that our modeling may be missing some aspects of the real experimental situation,[3] such as macroscopic solvent distribution and kinetic effects associated with loading of the analytes on the gold wires. The computations cannot currently reliably predict which enantiomer of a particular molecule will scatter the light more than the other. This would certainly significantly broaden the application field of SERS-ChA. Nevertheless, we find the modeling useful in providing a first insight into the fascinating phenomenon of chiral discrimination through resonance Raman scattering. The results are inspiring for further development of nanostructure and spectroscopic technologies.

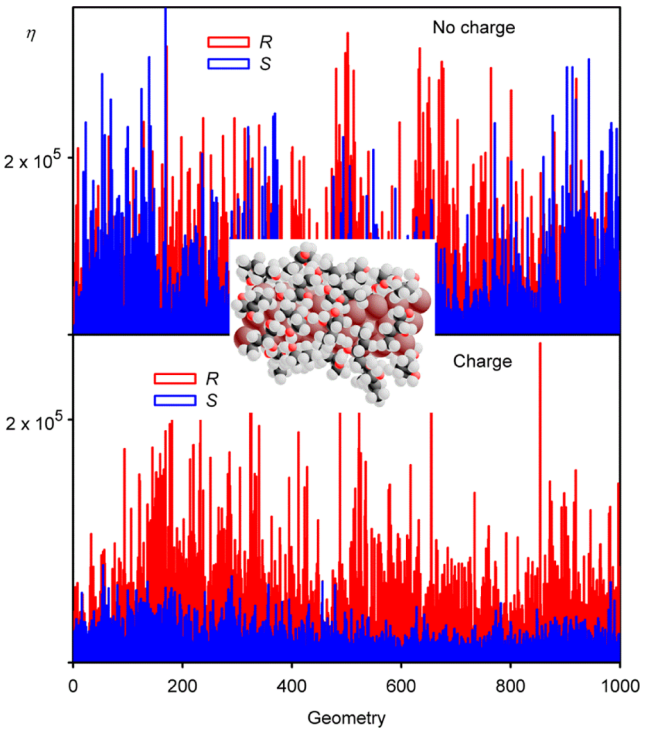

Figure 6. Effect of the gold self-polarization. Enhancement factors for 1000 snapshots of 1,2-butanediole and Au_{46} (example geometry in the center) were calculated without and with partial atomic charges on the gold atoms.

ASSOCIATED CONTENT

Supporting Information

The Supporting Information is available free of charge at https://pubs.acs.org/doi/10.1021/acs.jpcc.4c02703.

Additional computational results: chiral discrimination on a Au_{120} cluster, example of the dynamic electric intensity, tests of quantum chemical models for excited states, and dissymmetry factors for other chiral molecules (PDF)

Table 1. Enhancements (Including Statistical Error) and g-Factors Calculated with the Hückel Rigid Orbital Model for Selected Chiral SERS Systems

cluster	analyte	η_S	η_R	g
Au_{46}	1,2-butanediole	$(2.26 \pm 0.01) \times 10^4$	$(5.90 \pm 0.02) \times 10^4$	0.89
Au_{120}	1,2-butanediole	$(1.697 \pm 0.003) \times 10^5$	$(1.961 \pm 0.004) \times 10^5$	0.14
Au_{46}	phenylglycine	$(6.98 \pm 0.20) \times 10^4$	$(3.58 \pm 0.12) \times 10^4$	0.31
Au_{60}	glyceraldehyde	$(1.671 \pm 0.006) \times 10^5$	$(0.945 \pm 0.003) \times 10^5$	0.89
Au_{60}	1,2- epoxybutane	$(2.136 \pm 0.004) \times 10^5$	$(1.569 \pm 0.004) \times 10^5$	0.16

https://doi.org/10.1021/acs.jpcc.4c02703
J. Phys. Chem. C 2024, 128, 12649−12656

AUTHOR INFORMATION

Corresponding Author

Petr Bouř − *Institute of Organic Chemistry and Biochemistry, Academy of Sciences, 16610 Prague, Czech Republic; Department of Analytical Chemistry, University of Chemistry and Technology, 16628 Prague, Czech Republic;* orcid.org/0000-0001-8469-1686; Email: bour@uochb.cas.cz

Authors

Ondřej Škrna − *Institute of Organic Chemistry and Biochemistry, Academy of Sciences, 16610 Prague, Czech Republic*

Jiří Kessler − *Institute of Organic Chemistry and Biochemistry, Academy of Sciences, 16610 Prague, Czech Republic;* orcid.org/0000-0001-6307-4339

Zexi Liu − *School of Chemistry and Chemical Engineering, Shanghai Jiao Tong University, Shanghai 200240, P. R. China*

Shunai Che − *School of Chemistry and Chemical Engineering, Shanghai Jiao Tong University, Shanghai 200240, P. R. China;* orcid.org/0000-0001-7831-1552

Complete contact information is available at: https://pubs.acs.org/10.1021/acs.jpcc.4c02703

Notes

The authors declare no competing financial interest.

ACKNOWLEDGMENTS

The work was supported by the Grant Agency of the Czech Republic (22-04669S).

REFERENCES

(1) Pasteur, L. On the Relations Crystalline Form, Chemical Composition and Direction of Polarization Rotatorie. *Ann. Chim. Phys.* **1848**, *24*, 442−459.

(2) Barron, L. D. *Molecular Light Scattering and Optical Activity*; Cambridge University Press: Cambridge, UK, 2004.

(3) Liu, Z.; Ai, J.; Kumar, P.; You, E.; Zhou, X.; Liu, X.; Tian, Z.; Bouř, P.; Duan, Y.; Ding, S.; et al. Enantiomeric Discrimination by Surface-Enhanced Raman Scattering-Chiral Anisotropy of Chiral Nanostructured Gold Films. *Angew. Chem., Int. Ed.* **2020**, *59*, 15226−15231.

(4) Liu, Z.; Ai, J.; Bai, T.; Fang, Y.; Ding, K.; Duan, Y.; Han, L.; Che, S. Photomagnetic-Chiral Anisotropy of Chiral Nanostructured Gold Films. *Chem* **2022**, *8*, 186−196.

(5) Nafie, L. *Vibrational Optical Activity: Principles and Applications*; Wiley: Chichester, 2011.

(6) Schellman, J. A. Circular Dichroism and Optical Rotation. *Chem. Rev.* **1975**, *75*, 323−331.

(7) Charney, E. *The Molecular Basis of Optical Activity*; Wiley-Interscience: New York, 1979.

(8) Fasman, G. D. *Circular Dichroism and the Conformational Analysis of Biomolecules*; Plenum: New York, 1996.

(9) Lipparini, F.; Egidi, F.; Cappelli, C.; Barone, V. The Optical Rotation of Methyloxirane in Aqueous Solution: A Never Ending Story? *J. Chem. Theory Comput.* **2013**, *9*, 1880−1884.

(10) Krupová, M.; Kessler, J.; Bouř, P. Recent Trends in Chiroptical Spectroscopy: Theory and Applications of Vibrational Circular Dichroism and Raman Optical Activity. *ChemPlusChem* **2020**, *85*, 561−575.

(11) Abdali, S.; Blanch, E. W. Surface Enhanced Raman Optical Activity (Seroa). *Chem. Soc. Rev.* **2008**, *37*, 980−992.

(12) Das, M.; Gangopadhyay, D.; Šebestík, J.; Habartová, L.; Michal, P.; Kapitán, J.; Bouř, P. Chiral Detection by Induced Surface-Enhanced Raman Optical Activity. *Chem. Commun.* **2021**, *57*, 6388−6391.

(13) Zhu, Y.; He, J.; Shang, C.; Miao, X.; Huang, J.; Liu, Z.; Chen, H.; Han, Y. H. Chiral Gold Nanowires with Boerdijk−Coxeter−Bernal Structure. *J. Am. Chem. Soc.* **2014**, *136*, 12746−12752.

(14) Ding, S.-Y.; You, E.; Tian, Z.; Moskovits, M. Electromagnetic Theories of Surface-Enhanced Raman Spectroscopy. *Chem. Soc. Rev.* **2017**, *46*, 4042−4076.

(15) Atkins, P. W.; Friedman, R. S. *Molecular Quantum Mechanics*, 3rd ed.; Oxford University Press: New York, 1997.

(16) Krausbeck, F.; Autschbach, J.; Reiher, M. Calculated Resonance Vibrational Raman Optical Activity Spectra of Naproxen and Ibuprofen. *J. Phys. Chem. A* **2016**, *120*, 9740−9748.

(17) Li, G.; Alshalalfeh, M.; Yang, W.; Cheeseman, J. R.; Bouř, P.; Xu, Y. Can One Measure Resonance Raman Optical Activity? *Angew. Chem., Int. Ed.* **2021**, *60*, 22004−22009.

(18) Gill, P. M. W. Molecular Integrals over Gaussian Basis Functions. In *Advances in Quantum Chemistry*; Sabin, J. R.; Zerner, M. C., Eds.; Academic Press, Inc.: San Diego, 1994; Vol. 25, pp 142−205.

(19) Lebedev, V. I.; Laikov, D. N. Quadrature Formula for the Sphere of 131-Th Algebraic Order of Accuracy. *Dokl. Akad. Nauk.* **1999**, *366*, 741−745.

(20) Frisch, M. J.; Trucks, G. W.; Schlegel, H. B.; Scuseria, G. E.; Robb, M. A.; Cheeseman, J. R.; Scalmani, G.; Barone, V.; Petersson, G. A.; Nakatsuji, H.et al. *Gaussian 16 Rev. A.03*; Gaussian, Inc.: Wallingford, CT, 2016.

(21) Becke, A. D. Density-Functional Thermochemistry. Iii. The Role of Exact Exchange. *J. Chem. Phys.* **1993**, *98*, 5648−5652.

(22) Chiodo, S.; Russo, N.; Sicilia, E. Lanl2dz Basis Sets Recontracted in the Framework of Density Functional Theory. *J. Chem. Phys.* **2006**, *125*, No. 104107.

(23) Figgen, D.; Rauhut, G.; Dolg, M.; Stoll, H. Energy-Consistent Pseudopotentials for Group 11 and 12 Atoms: Adjustment to Multi-Configuration Dirac-Hartree-Fock Data. *Chem. Phys.* **2005**, *311*, 227−244.

(24) Foresman, J. B.; Head-Gordon, M.; Pople, J. A.; Frisch, M. J. Toward a Systematic Molecular Orbital Theory for Excited States. *J. Phys. Chem. A* **1992**, *96*, 135−149.

(25) Stewart, J. J. P. Optimization of Parameters for Semiempirical Methods Vi: More Modifications to the Nddo Approximations and Re-Optimization of Parameters. *J. Mol. Model.* **2013**, *19*, 1−32.

(26) Hoffmann, R. An Extended Hückel Theory. I. Hydrocarbons. *J. Chem. Phys.* **1963**, *39*, 1397−1412.

(27) Ponder, J. W. *Tinker, Software Tools for Molecular Design*, 3.8rd ed.; Washington University School of Medicine: Saint Louis, 2000.

(28) Case, D. A.; Cheatham, I. T. E.; Darden, T.; Gohlke, H.; Luo, R.; Merz, J. K. M.; Onufriev, A.; Simmerling, C.; Wang, B.; Woods, R. The Amber Biomolecular Simulation Programs. *J. Comput. Chem.* **2005**, *26*, 1668−1688.

(29) Singh, U. C.; Kollman, P. A. An Approach to Computing Electrostatic Charges for Molecules. *J. Comput. Chem.* **1984**, *5*, 129−145.

(30) Kim, J.-Y.; Yeom, J.; Zhao, G.; Calcaterra, H.; Munn, J.; Zhang, P.; Kotov, N. Assembly of Gold Nanoparticles into Chiral Superstructures Driven by Circularly Polarized Light. *J. Am. Chem. Soc.* **2019**, *141*, 11739−11744.

(31) Montaño-Priede, J. L.; Pal, U. Estimating near Electric Field of Polyhedral Gold Nanoparticles for Plasmon-Enhanced Spectroscopies. *J. Phys. Chem. C* **2019**, *123*, 11833−11839.

(32) Liu, W.; Wang, C.; Ding, H.; Shao, J.; Ding, Y. Ac Electric Field Induced Dielectrophoretic Assembly Behavior of Gold Nanoparticles in a Wide Frequency Range. *Appl. Surf. Sci.* **2016**, *370*, 184−192.

(33) Chen, T.; Wang, D.; Wan, L. J. Two-Dimensional Chiral Molecular Assembly on Solid Surfaces: Formation and Regulation. *Natl. Sci. Rev.* **2015**, *2*, 205−216.